Article | Received 28 January 2026; Revised 6 April 2026; Accepted 10 April 2026; Published 28 May 2026
https://doi.org/10.55092/mt20260001

Reconstruction of helicopter rotor pressure fields using physics-informed neural networks and flexible pressure sensor arrays

Tong Qu and Ke Sun*

Institute of Testing Technology, Chinese Flight Test Establishment, Xi'an 710089, China

* Correspondence author; E-mail: ke_sunedu@163.com.

Highlights:

- Kriging regression builds sparse-sensor pressure priors + uncertainty variance maps.
- K-PINN couples PINN with Kriging uncertainty-weighted loss for reconstruction.
- Sensitivity analysis pinpoints leading edge & tip as key sensor placement zones.

Abstract: To address the challenges of inaccessible pressure data on helicopter blade surfaces and the inability of sparse pressure measurement points to fully characterize the pressure field across the entire blade, this paper proposes a rotor-blade surface pressure reconstruction framework that combines flexible pressure sensing arrays, Kriging-based statistical priors, and physics-informed neural networks (PINNs). First, a scaled rotor experimental platform equipped with a flexible pressure sensor array is developed to acquire full-field reference pressure data under multiple rotational speeds, providing a verifiable benchmark for model training and evaluation. Under sparse sensing conditions, Kriging regression is then used to generate a prior pressure field together with a spatial variance map that quantifies uncertainty in unmeasured regions. Based on this prior, a residual-learning PINN is constructed, in which weak physical constraints are incorporated into the loss function, while the Kriging variance is further used to achieve spatially adaptive weighting between data fidelity and physics regularization. The main contribution of the proposed framework lies in the integration of statistical prior modeling, uncertainty-aware physics coupling, and flexible-array-based experimental benchmarking for rotor-specific pressure reconstruction. Experimental results show that the proposed method achieves accurate full-field reconstruction under sparse measurements, with an overall reconstruction error of approximately 4%, while preserving key pressure features in critical regions such as the leading edge and blade tip. In addition, sensitivity analysis indicates that the leading-edge and tip regions are the most critical to global reconstruction accuracy, providing practical guidance for sensor placement.

Keywords: pressure field reconstruction; physics-informed neural network; flexible sensing array; helicopter rotor; Kriging

Copyright©2026 by the authors. Published by ELSP. This work is licensed under Creative Commons Attribution 4.0 International License, which permits unrestricted use, distribution, and reproduction in any medium provided the original work is properly cited.

1. Introduction

1.1. Research background

As a key piece of equipment with vertical take-off and landing (VTOL) and low-altitude high-maneuverability capabilities, the helicopter is indispensable in specialized scenarios such as military operations, emergency rescue, and high-altitude material transport. Throughout its research and development process, flight testing is the crucial link for verifying performance and exploring the flight envelope. Particularly in the finalization test flight stage, the proportion of aerodynamic performance verification for the rotor system is significantly higher than for fixed-wing aircraft. However, the flight test environment differs from that of a wind tunnel; variables such as airflow and temperature cannot be controlled. The rotor not only experiences flapping and lead-lag motions under high-speed rotation but also contends with complex conditions like ground effect and crosswind interference, making the aerodynamic flow field more difficult to capture. Concurrently, flight testing imposes extremely high safety requirements. Any pressure measurement technique that compromises the structural integrity of the blade or introduces flow field disturbances could pose a flight risk, placing stringent demands on the non-destructive nature and reliability of the measurement solution.

Accurately obtaining the surface pressure distribution on a rotor blade is the primary means of evaluating rotor performance and identifying aerodynamic hazards during flight tests, and it relies on full-surface pressure measurements. The pressure distribution in different regions of the blade corresponds to distinct aerodynamic characteristics: the pressure gradient at the leading edge directly determines lift generation efficiency, the pressure transition in the mid-to-trailing-edge region reflects the flow attachment state, and the pressure distribution at the blade tip is associated with the intensity and influence range of the tip vortex. Only by acquiring full-surface pressure data can the complete rotor flow field be fully reconstructed, allowing for the precise calculation of key performance indicators such as the lift-to-drag ratio and power requirements. This provides comprehensive support for load assessment and the definition of a safe operating envelope, while also validating the accuracy of full-field simulation results and guiding the global optimization of the blade's aerodynamic shape.

Simultaneously, the implementation of full-surface pressure measurement faces a threefold challenge. First, the high-speed rotation of the blade is accompanied by flapping and lead-lag motions, as well as non-linear deformations arising from the coupled effects of centrifugal and aerodynamic forces. This requires the pressure measurement technology to possess excellent dynamic adaptability to accurately capture pressure changes at various locations as the blade moves. Second, to ensure flight test safety, the measurement technique must be non-destructive. Any method that compromises the structural integrity of the blade could affect its stiffness and aerodynamic profile, thereby introducing additional flow field disturbances. Third, full-surface measurement must cover all areas of the blade, from root to tip and from leading to trailing edge. Traditional pressure measurement techniques are either limited to sparse measurement points due to spatial constraints, failing to cover the entire surface, or are unable to achieve stable measurements across all regions due to technical limitations. As a result, simultaneously meeting the three requirements of dynamic adaptability, non-destructive measurement, and full-surface coverage has remained a persistent challenge, making the acquisition of full-surface pressure data a key bottleneck in flight testing.

The precise measurement of surface pressure fields is a cornerstone of modern aerodynamic research, crucial for revealing complex flow mechanisms, validating numerical computation models, and optimizing aircraft aerodynamic design. Its role is particularly indispensable in the aerodynamic analysis of high-speed rotating components such as helicopter rotors and turbine cascades [1–3]. Traditional pressure measurement techniques primarily rely on contact-based methods, where pressure taps are drilled into the model surface and connected to pressure sensors via tubes. However, extensive research and engineering practice have shown that such methods have inherent and insurmountable drawbacks. Firstly, the installation of pressure taps is physically intrusive, disturbing the local flow field and potentially inducing unintended flow separation or transition, thereby contaminating the accuracy of the measurement data [4]. Secondly, due to considerations of structural integrity and limited internal space, the number and density of pressure taps are severely restricted, resulting in sparse, discrete data that cannot capture the complete characteristics of the global pressure distribution [5]. More critically, the pressure tube system introduces significant signal delays and frequency response attenuation, making it inadequate for measuring high-speed, unsteady flow phenomena such as dynamic stall and shock wave oscillations [6].

To fundamentally overcome the bottlenecks of contact-based measurements and achieve global, high-resolution, and non-intrusive pressure measurement, researchers have turned to optical measurement techniques. Among them, the emergence and development of pressure-sensitive paint (PSP) technology represents a revolutionary breakthrough in the field [7,8]. This technology leverages the principle that the luminescence intensity of specific fluorescent molecules is modulated by oxygen partial pressure (the oxygen quenching effect). By applying a thin layer of paint to the model surface, the complex problem of pressure field measurement is transformed into an analysis of the luminescence intensity of captured images, thereby yielding a detailed, full-field pressure distribution [9,10]. Liu *et al.* conducted in-depth studies on the dynamic characteristics of PSP, developing fast-response PSP suitable for unsteady flow field testing [11,12]. Numerous researchers, both domestically and internationally, have utilized PSP technology to conduct highly effective studies on various complex flow problems. For instance, Watkins and Leighty *et al.* successfully applied PSP to high-speed rotating helicopter rotor blades, clearly capturing tip vortices and transonic shock wave structures [13]. Chen and Zhu *et al.* used PSP to quantitatively evaluate fine flow details such as film cooling effectiveness and hole shape effects on turbine blade leading edges [14,15].

Despite its tremendous success, PSP technology also faces its own challenges. For example, the temperature sensitivity of the luminescent signal requires complex corrections, the photochemical degradation of the coating affects long-term test stability, and its application in harsh environments remains limited [11,16]. Concurrently, rapid advancements in materials science and micro/nano-fabrication have given rise to flexible electronics technology, offering a new paradigm for pressure measurement. Represented by the research of Cheng and Wang *et al.*, flexible capacitive or piezoresistive pressure sensors based on new materials (e.g., PDMS/graphene) and microstructural designs offer unique advantages such as being lightweight, thin, and conformally attachable [17–20]. These sensors can be seamlessly integrated with complex curved surfaces like a second “skin”, holding the potential for large-scale, high-density, distributed in-situ pressure measurement and demonstrating capabilities that surpass traditional measurement techniques in specific scenarios [21,22].

Whether dealing with sparse traditional measurement points or high-density PSP pixels or flexible sensor arrays, the reconstruction of a continuous, complete, and accurate pressure field from discrete measurement data remains a critical aspect of pressure measurement technology. Traditional reconstruction methods, such as those based on velocity field integration (from PIV/PTV) or the virtual field method, often suffer from error accumulation or a reliance on specific basis functions [23–25]. To more efficiently utilize sparse measurement information, reconstruction methods based on Compressed Sensing have been proposed. Research by Qiu and Sun *et al.* has shown that this method can accurately recover a pressure field from a small number of measurement points under certain conditions, but its effectiveness is highly dependent on the assumption of sparsity in a specific transform domain and the optimization of sensor placement [26,27].

In recent years, artificial intelligence technologies, particularly deep learning, have provided powerful tools for solving this high-dimensional, non-linear reconstruction problem. Numerous studies have demonstrated that by training neural networks on large amounts of high-fidelity data, it is possible to construct a rapid mapping model from sparse measurement points to the full-domain flow field [28–30]. However, purely data-driven deep learning models have their own set of problems. In their review, Huang *et al.* explicitly stated that the generalization ability of such models is limited; that is, their prediction accuracy deteriorates sharply when the actual flow conditions deviate from the training dataset [31,32]. More importantly, as a "black box", their predictions may not satisfy the fundamental physical conservation laws of fluid flow (e.g., the Navier-Stokes equations), leading to results that lack physical credibility [33,34].

To overcome the lack of physical consistency and the dependence on massive datasets inherent in purely data-driven methods, Raissi, Karniadakis, and colleagues pioneered Physics-Informed Neural Networks (PINN) [35]. PINN embeds the governing equations of fluid dynamics as a penalty term in the neural network's loss function, thereby imposing physical constraints on the model while it learns from data. This framework ensures the physical self-consistency of the reconstruction results and significantly reduces the demand for labeled data, opening up a new paradigm for solving scientific computing and data fusion problems under "small data" conditions [36].

1.2. Proposed solution and innovations

Although PINNs have been widely studied for inverse field reconstruction, the present work does not claim novelty in the use of PINNs alone. Instead, this study focuses on the specific engineering problem of sparse pressure-field reconstruction on helicopter rotor blades, where limited sensor coverage, strong local gradients, and cross-operating-condition generalization make direct application of existing reconstruction methods insufficient.

To address these challenges, this paper proposes a rotor-oriented hybrid reconstruction framework that integrates flexible pressure sensing arrays, Kriging-based statistical prior modeling, and uncertainty-aware physics-informed learning. The main contribution of this work lies in the coordinated integration of the following components rather than in introducing a fundamentally new generic PINN architecture:

Full-field benchmark construction based on a flexible pressure sensor array.

A scaled rotor experimental platform is developed to obtain full-field pressure data under multiple rotational speeds. These measurements provide a verifiable benchmark for model training and evaluation,

while fixed sparse sensing configurations are extracted from the full-field data to emulate engineering measurement constraints.

Kriging-based prior modeling with spatial uncertainty quantification.

Sparse pressure measurements are first used to generate a continuous prior pressure field through Kriging regression. At the same time, the corresponding spatial variance is obtained as an uncertainty map, which explicitly characterizes the confidence level in unmeasured regions.

Uncertainty-aware K-PINN framework for rotor pressure reconstruction.

Based on the Kriging prior, a residual-learning PINN is constructed, in which weak physical and geometric constraints relevant to rotor surface pressure reconstruction are embedded into the loss function. Moreover, the Kriging variance is used to achieve spatially adaptive weighting between data fidelity and physics regularization, thereby improving training robustness and physical consistency under sparse sensing conditions.

Rotor-specific validation and sensor placement analysis.

The proposed framework is systematically validated for helicopter rotor blade pressure reconstruction through full-field error evaluation, critical-region feature preservation analysis, and sensitivity studies of sparse measurement locations. The results further identify the leading-edge and tip regions as the most influential zones for reconstruction accuracy, providing practical guidance for sensor placement in future applications.

Therefore, the novelty of this study lies in a task-oriented integration of statistical prior modeling, uncertainty-aware physics coupling, flexible-array-based experimental benchmarking, and rotor-specific validation.

2. Methods

The technical approach of this study follows a systematic fusion strategy. Rather than relying on a standard physics-informed formulation alone, the present framework incorporates Kriging-derived priors, spatial uncertainty information, and rotor-relevant weak physical constraints to improve reconstruction under sparse measurements.

First, full-field reference pressure data under multiple rotational-speed conditions are obtained using a flexible pressure sensor array, from which 15 fixed key measurement points are extracted to emulate sparse engineering measurements.

Second, under sparse sensing conditions, Kriging regression is used to generate a continuous prior pressure field $p_K(\tilde{x}, \tilde{y} \mid \omega)$ over the valid blade domain, while simultaneously providing a spatial variance field σ_K^2 to characterize the relative confidence level in unmeasured regions.

Third, based on this prior, a residual-learning neural reconstruction framework is established, in which the network focuses on learning the deviation between the Kriging prior and the target full-field pressure distribution, rather than reconstructing the entire field from scratch. To improve reconstruction stability and physical plausibility, weak physical and structural constraints consistent with the surface-pressure field are incorporated into the loss function, including continuity-related regularization, geometric boundary stabilization, and structure-preserving constraints in sensitive regions.

In addition, the Kriging variance is mapped into a spatial weight field, which is synchronously applied to the supervised term and the physical residual term so as to strengthen correction in high-uncertainty regions while avoiding overcorrection in reliable regions. On this basis, a Kriging-enhanced physics-informed

neural network (K-PINN) is constructed to output a continuous full-surface pressure field $p_{K-PINN}(\tilde{x}, \tilde{y} \mid \omega)$, achieving stable and accurate reconstruction under sparse measurements while maintaining consistency with the statistical prior, experimental reference data, and weak physical constraints. Figure 1 is the reconstruction technical roadmap of this paper.

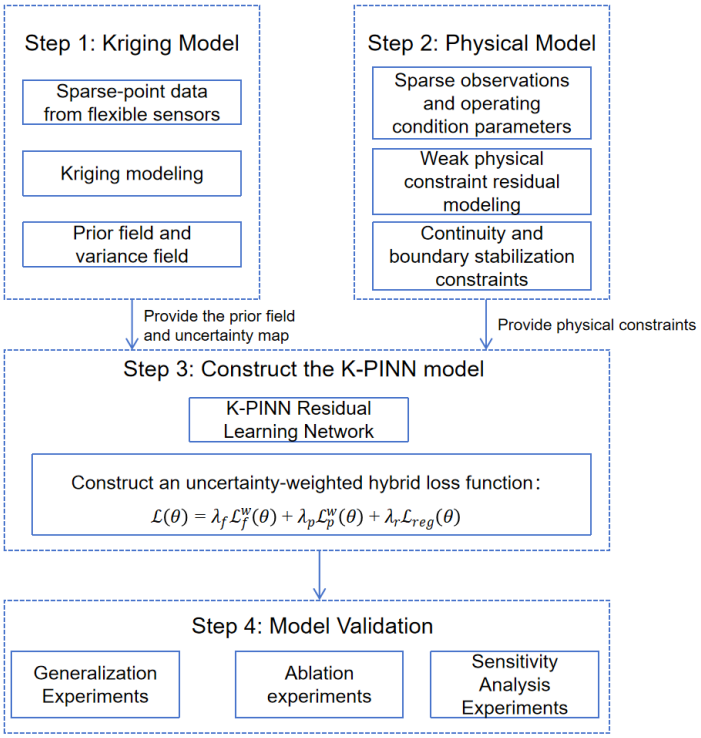

Figure 1. Technical roadmap for pressure field reconstruction on helicopter rotor blades based on K-PINN.

2.1. Kriging interpolation

Kriging interpolation, also known as spatial auto-covariance optimal interpolation, is a method for linear optimal, unbiased interpolation estimation of spatially distributed pressure data on helicopter rotors. This method uses sample data at different spatial locations and varying degrees of spatial correlation between samples to assign corresponding weights to each sample. It estimates the pressure value at unknown points through a sliding weighted average. Kriging interpolation utilizes the original observational data of regionalized pressure variables and the structural characteristics revealed by the variogram to perform linear unbiased optimal estimation of regionalized pressure variable values at unsampled points. The Kriging interpolation method for helicopter rotor pressure fields includes three important concepts: regionalized pressure variable, variogram, and covariance function.

This study introduces a Kriging statistical model to extend sparse measurement information. For each rotational-speed condition, the mean pressures at 15 key measurement points are used as inputs to generate a full-field prior mean pressure field over the valid blade domain, while the corresponding prediction variance is also provided to characterize the spatial distribution of uncertainty. The purpose of this section is not to reproduce the entire blade pressure field with full fidelity under sparse sensing conditions, but rather to provide a stable initial estimate with reasonable spatial continuity, *i.e.*, a statistical prior, so that the subsequent model does not need to generate the full-field pressure distribution

from scratch, thereby improving reconstruction efficiency. The variance field is further used as an uncertainty map to indicate the reliability of predictions in different regions.

2.1.1. Model selection

Considering that the Kriging model in this study takes only 15 sparse points as inputs, and given the purpose of this section, Ordinary Kriging (OK) is adopted for the following reasons:

(1) Only 15 sparse points are available. If an explicit trend term, as in Universal Kriging, were introduced, additional trend coefficients would need to be estimated, which could easily lead to parameter coupling and unstable priors under such a small-sample setting.

(2) This chapter requires an uncertainty map. OK naturally provides prediction variance while producing the mean prediction, which is consistent with the objective of this section.

(3) The Kriging model in this study is not intended to recover fine-scale details through interpolation alone. Scale differences can be discussed later through the reconstruction results in different regions, while fine corrections are delegated to the physical constraints and residual learning of K-PINN.

2.1.2. Characterization of spatial correlation

The key to Kriging lies in establishing the spatial correlation structure. First, a discrete variogram is estimated from the samples, and then a continuous variogram model is fitted.

(1) Coordinate normalization and anisotropic distance

The spanwise and chordwise geometric scales of the blade are different. Therefore, nondimensionalization is applied here, and an anisotropic distance is adopted:

$$d_{ij} = \sqrt{\left(\frac{\tilde{x}_i - \tilde{x}_j}{\ell_x}\right)^2 + \left(\frac{\tilde{y}_i - \tilde{y}_j}{\ell_y}\right)^2} \tag{1}$$

where ℓ_x and ℓ_y are the hyperparameters controlling the correlation scales in the spanwise and chordwise directions, respectively. This setting allows the pressure field to have a shorter correlation length in the chordwise direction than in the spanwise direction, thereby preventing the global model from oversmoothing the leading-edge gradient region.

(2) Variogram model selection: Gaussian model with nugget effect

In this study, a Gaussian variogram model is used as the baseline, with an explicit nugget term:

$$\gamma(h) = C_0 + C[1 - \exp(-(h/a)^2)] \tag{2}$$

where C_0 is the nugget effect, C is the structural variance, and a is the range, while h is given by the anisotropic distance defined above. The main motivation for choosing the Gaussian model is to serve the prior-generation task of this study. The Gaussian model provides stronger smoothness and can generate a more stable prior mean field under the sparse constraint of only 15 points.

(3) Parameter fitting strategy: offline calibration and reuse across operating conditions

If the model were refitted for each rotational-speed condition using only 15 points, the results would be highly sensitive to measurement noise and local gradients, leading to unstable priors. Taking advantage of the fact that full-field reference data is available experimentally, this study adopts a two-stage strategy:

Calibration stage: empirical variogram curves are estimated from the full-field mean pressure full-field reference data over the training-speed set and then fitted with a continuous model. The final model form is fixed as Gaussian + nugget + anisotropy, with a reasonable parameter range determined accordingly.

Generation stage: for any operating condition, the mean pressures at the 15 sparse points are directly used as input, and the weights are solved under fixed hyperparameters to output $p_K(\mathbf{s}_0|\omega)$ and $\sigma_K^2(\mathbf{s}_0|\omega)$.

It should be emphasized that, in the calibration stage, the empirical variogram computed from the full-field mean pressure full-field reference data over the training-speed set is not used to learn or memorize the deterministic spatial distribution of the pressure field for a specific condition. Rather, it is used to calibrate the spatial statistical correlation structure of the pressure field. This process is an offline statistical calibration of the Kriging hyperparameters, intended to improve the stability and reproducibility of prior generation.

2.1.3. Weight solution and prediction variance output

After the spatial correlation model is determined and the hyperparameters are fixed, the next step is to generate the full-field prior mean field and prediction variance field for a single rotational-speed condition based on the steady-state mean pressures at the 15 sparse measurement points.

(1) Kriging estimator and unbiasedness constraint

Under the Ordinary Kriging framework, the pressure random field can be written as:

$$\mathrm{p}(\mathrm{x},\mathrm{y}) = \mathrm{m} + \varepsilon(\mathrm{x},\mathrm{y}) \tag{3}$$

where mu is the locally constant mean term, and epsilon(x) is a zero-mean random perturbation describing the spatial correlation structure. For a target location x, the Ordinary Kriging linear unbiased estimator is written as:

$$\hat{\mathrm{p}}(\mathrm{s}_0) = \sum_{\mathrm{i}=1}^{\mathrm{K}} \lambda_\mathrm{i}\, \mathrm{p}(\mathrm{s}_\mathrm{i}) \tag{4}$$

subject to the unbiasedness constraint:

$$\sum_{\mathrm{i}=1}^{\mathrm{K}} \lambda_\mathrm{i} = 1 \tag{5}$$

The weights λ_i are determined by the minimum estimation-variance criterion, they minimize the estimation error $\mathrm{Var}[\hat{p}(\mathbf{s}_0) - p(\mathbf{s}_0)]$ under the unbiasedness constraint.

(2) Weight solution: minimum-variance-unbiased criterion and linear system

Using the Lagrange multiplier method, the Ordinary Kriging system can be obtained as:

$$\begin{bmatrix} \Gamma & \mathbf{1} \\ \mathbf{1}^{\mathrm{T}} & 0 \end{bmatrix} \begin{bmatrix} \boldsymbol{\lambda} \\ \mu \end{bmatrix} = \begin{bmatrix} \boldsymbol{\gamma}_0 \\ 1 \end{bmatrix} \tag{6}$$

where Γ is the semivariance matrix between all sparse measurement points, $\boldsymbol{\gamma}_0$ is the semivariance vector between the sparse points and the target point, and μ is the Lagrange multiplier. The semivariogram adopts the Gaussian form with a nugget term.

(3) Prediction variance output: formation and interpretation of the confidence map

After solving for the weights $\boldsymbol{\lambda}$ and Lagrange multipliers μ, the prediction variance at the target point can be obtained simultaneously. In semivariance form, it is commonly expressed as:

$$\sigma_K^2(s_0) = \lambda^T \gamma_0 + \mu \tag{7}$$

This variance is jointly determined by the spatial distribution of the measurement points and the correlation structure, and can therefore be used as a unified quantitative indicator of spatial uncertainty.

2.1.4. Parameter settings

The final adopted spatial correlation model is written as:

$$\gamma(h) = C_0 + C\left[1 - \exp\left(-\left(\frac{h}{a}\right)^2\right)\right], \quad h = \sqrt{\left(\frac{\Delta\tilde{x}}{\ell_x}\right)^2 + \left(\frac{\Delta\tilde{y}}{\ell_y}\right)^2} \tag{8}$$

For the representative operating condition of 285 rpm, the fitted correlation parameters are as follows, Table 1 lists the Kriging fitting parameters under the 285 rpm condition.

Table 1. Fitted correlation parameters for the 285 rpm condition.

Parameter	Symbol	Value	Unit
Constant mean	m	/	kPa
Structural variance	C	0.045	kPa^2
Nugget effect	C_0	0.004	kPa
Sill	$C_0 + C$	0.049	kPa^2
Spanwise correlation scale	ℓ_x	0.12	/
Chordwise correlation scale	ℓ_y	0.28	/

2.2. Construction of the PINN residual structure and loss function

To inherit the global stability of the Kriging prior while concentrating the correction on its deviations in sensitive regions, this study adopts a prior-guided residual representation:

$$p_{K-PINN}(\tilde{x}, \tilde{y} \mid \omega) = p_K(\tilde{x}, \tilde{y} \mid \omega) + \Delta p_\theta(\tilde{x}, \tilde{y}, \omega) \tag{9}$$

where $p_K(\tilde{x}, \tilde{y} \mid \omega)$ denotes the prior mean field, Δp_θ denotes the correction term learned by the neural network, and θ represents the network parameters. The training of K-PINN follows three basic principles: supervised consistency, physical consistency, and stability regularization.

2.2.1. Full-field supervised loss during training (data term)

The experimental data in this study provide steady-state mean pressure fields with full-coverage array measurements under different operating conditions. In order to fully exploit this information during training and improve the efficiency of mapping learning, a discrete point set is selected within the valid domain $\Omega_N = \{\mathbf{r}_j\}_{j=1}^N$ (approximately 3000 discrete points for a single operating condition), and the full-field supervised loss is defined as:

$$\mathcal{L}_f(\theta) = \frac{1}{N}\sum_{j=1}^{N}\left(p_{K-PINN}(r_j \mid \omega) - \bar{p}(r_j \mid \omega)\right)^2 \tag{10}$$

2.2.2. Physical residual loss

Under the problem setting of this study, the observable inputs of the model consist of the fixed 15-point sparse pressure observations and the operating-condition parameters. Although the full-field steady-state mean pressure field is available during training, the data do not include high-dimensional flow information such as velocity fields, density fields, or boundary-layer profile variables. Therefore, the construction of the physical constraints does not aim to solve the full Navier-Stokes equations, but instead adopts weak physical and structural control relations that are consistent with the surface pressure field as a continuous physical field, so that the reconstructed pressure field maintains reasonable continuity, scale consistency, and boundary stability on the geometric surface.

Combined with the anisotropic scale information provided by the Kriging prior, this study employs an anisotropic screened *Poisson/Helmholtz-type* weak constraint as the physical residual operator. Its basic form is written as:

$$\mathcal{R}[\mathrm{p_{K-PINN}}](\tilde{\mathrm{x}},\tilde{\mathrm{y}},\omega) = -\left(\kappa_{\mathrm{x}}\frac{\partial^2 \mathrm{p_{K-PINN}}}{\partial \tilde{\mathrm{x}}^2} + \kappa_{\mathrm{y}}\frac{\partial^2 \mathrm{p_{K-PINN}}}{\partial \tilde{\mathrm{y}}^2}\right) + \mu\ \mathrm{p_{K-PINN}} - \mathrm{s}(\tilde{\mathrm{x}},\tilde{\mathrm{y}},\omega) \tag{11}$$

where κ_x, κ_y are spatial scale coefficients used to reflect the difference between the correlation scales in the spanwise and chordwise directions, respectively; $\mu \geq 0$ is the screening coefficient used to suppress drift in weakly constrained regions; and $s(\tilde{x}, \tilde{y}, \omega)$ represents the source term corresponding to the driving effect induced by the aerodynamic load distribution. Within the PINN framework, the residual in the above expression can be computed by automatic differentiation of second-order derivatives only, without relying on unobservable variables such as velocity.

To avoid over-smoothing the pressure field and thereby losing necessary real structures, the source term $s(\tilde{x}, \tilde{y}, \omega)$ is represented in a learnable form. It is treated as an unknown driving term varying with space and operating condition, represented by a lightweight source function and jointly determined together with the supervised term during training. The physical meaning of this treatment is that the overall pressure field satisfies anisotropic smooth propagation and screened stability constraints, while the true local loading and gradients are characterized by the source term.

In this study, κ_x, κ_y are linked to the corresponding correlation-length scales. Here, $\kappa_x \propto \ell_x^2$ 、 $\kappa_y \propto \ell_y^2$ are adopted, so that when the chordwise correlation length is larger, the scale constraint associated with the chordwise second-derivative term becomes correspondingly stronger.

Given the inherent boundaries of the effective measurement domain, weak boundary constraints with zero normal gradients are imposed on $\partial\Omega$ to suppress extrapolation artifacts and non-physical spikes near the boundaries:

$$\mathcal{R}_{\mathrm{b}}[\mathrm{p_{K-PINN}}] = \frac{\partial \mathrm{p_{K-PINN}}}{\partial \mathrm{n}} \approx 0, \quad (\tilde{\mathrm{x}},\tilde{\mathrm{y}}) \in \partial\Omega, \tag{12}$$

where n denotes the outward unit normal vector on the boundary. This constraint can be understood as a treatment that avoids imposing excessively steep variations toward unknown regions outside the boundary, and it helps reduce the risk of oscillation near the mask boundary.

Accordingly, the physical residual loss is defined on the set of collocation points $\mathcal{C} = \{\mathbf{c}_j\}_{j=1}^{N_c} \subset \Omega$ as:

$$\mathcal{L}_{\mathrm{p}}(\theta) = \frac{1}{\mathrm{N_c}}\sum_{\mathrm{j=1}}^{\mathrm{N_c}} \left\|\mathcal{R}[\mathrm{p_{K-PINN}}](\mathrm{c_j},\omega)\right\|^2 + \beta_{\mathrm{b}}\ \frac{1}{\mathrm{N_b}}\sum_{\mathrm{k=1}}^{\mathrm{N_b}} \left\|\mathcal{R}_{\mathrm{b}}[\mathrm{p_{K-PINN}}](\mathrm{c_{b,k}},\omega)\right\|^2 \tag{13}$$

where N_c、N_b denote the numbers of collocation points and boundary points, respectively, and β_b is the proportionality coefficient of the boundary term. This physical term is synchronously weighted together with the uncertainty weight field, so that regions with higher uncertainty receive stronger constraints in both supervised consistency and physical plausibility.

2.2.3. Residual regularization term

Under the residual-learning paradigm based on prior plus correction, the correction term Δp_θ should mainly compensate for the deviation of the statistical prior in extrapolated regions, rather than introduce excessive perturbations in areas where the prior is reliable. To enhance training stability and reduce the risk of overfitting, a residual-energy regularization term is adopted:

$$\mathcal{L}_{\mathrm{reg}}(\theta) = \frac{1}{\mathrm{N_c}} \sum_{\mathrm{j=1}}^{\mathrm{N_c}} \left| \Delta \mathrm{p}_\theta(\mathrm{c_j} \mid \omega) \right|^2 \tag{14}$$

2.2.4. Total loss function

By combining the above three types of constraints, the joint loss function defined in this chapter is:

$$\mathcal{L}(\theta) = \lambda_{\mathrm{f}} \mathcal{L}_{\mathrm{f}}(\theta) + \lambda_{\mathrm{p}} \mathcal{L}_{\mathrm{p}}(\theta) + \lambda_{\mathrm{r}} \mathcal{R}_{\mathrm{reg}}(\theta) \tag{15}$$

2.3. Spatially adaptive weighting strategy based on uncertainty

As shown by the variance-error consistency analysis presented later, σ_K^2 exhibits a stable ability to rank the relative confidence level in space. In regions where the measurement-point constraint is weaker and the extrapolation risk is higher, the prediction variance is usually larger and better indicates the concentration of reconstruction errors. Based on this empirical observation, this study maps σ_K^2 into a spatial weight field and applies it simultaneously to the full-field supervised term and the physical residual term, so as to strengthen correction in risk-prone regions while avoiding excessive perturbation in reliable regions.

2.3.1. Variance normalization and construction of the weight field

Because the magnitude of the prediction variance differs across operating conditions, direct use of the raw variance would make the weights incomparable between conditions. Therefore, a condition-wise normalized uncertainty indicator is constructed as:

$$\hat{\sigma}(\tilde{\mathrm{x}}, \tilde{\mathrm{y}} \mid \omega) = \frac{(\tilde{\mathrm{x}}, \tilde{\mathrm{y}} \mid \omega) - \sigma^2_{\mathrm{min}}(\omega)}{\sigma^2_{\mathrm{max}}(\omega) - \sigma^2_{\mathrm{min}}(\omega) + \varepsilon} \tag{16}$$

where σ^2_{min} and σ^2_{max} are the minimum and maximum variance values within the valid domain under a given operating condition, respectively, and ε is a numerical stabilization constant. The normalized uncertainty indicator is then mapped into a weight field:

$$\mathrm{w}(\tilde{\mathrm{x}}, \tilde{\mathrm{y}} \mid \omega) = \mathrm{w_{min}} + \alpha\, \hat{\sigma}(\tilde{\mathrm{x}}, \tilde{\mathrm{y}} \mid \omega), \tag{17}$$

and an upper truncation is imposed to ensure optimization stability:

$$\mathrm{w}(\tilde{\mathrm{x}}, \tilde{\mathrm{y}} \mid \omega) = \min(\mathrm{w}(\tilde{\mathrm{x}}, \tilde{\mathrm{y}} \mid \omega),\ \mathrm{w_{max}}) \tag{18}$$

In the above construction, $w_{\min}$ ensures that low-uncertainty regions still retain a basic supervised strength; α controls the degree of amplification in risk-prone regions; and $w_{\max}$ is used to prevent extremely high-variance points from generating excessively large gradients during backpropagation and dominating the training process. Because this weight depends only on the Kriging output and its relative validity is verified later, its role is to allocate learning resources rather than to equate variance with a pointwise estimate of error.

2.3.2. Synchronous spatial weighting of the supervised and physical terms

After the weight field is determined, the full-field supervised loss is rewritten in a spatially weighted form:

$$\mathcal{L}_{\mathrm{f}}^{\mathrm{w}}(\theta)=\frac{1}{\mathrm{N}}\sum_{\mathrm{j}=1}^{\mathrm{N}}\mathrm{w}\left(\mathrm{r}_{\mathrm{j}}\mid\omega\right)\left(\mathrm{p}_{\mathrm{K-PINN}}\left(\mathrm{r}_{\mathrm{j}}\mid\omega\right)-\bar{\mathrm{p}}\left(\mathrm{r}_{\mathrm{j}}\mid\omega\right)\right)^{2} \tag{19}$$

Correspondingly, the physical residual term is also weighted using the same weight field:

$$\mathcal{L}_{\mathrm{p}}^{\mathrm{w}}(\theta)=\frac{1}{\mathrm{N_c}}\sum_{\mathrm{j}=1}^{\mathrm{N_c}}\mathrm{w}\left(\mathrm{c}_{\mathrm{j}}\mid\omega\right)\parallel\mathcal{R}[\mathrm{p}_{\mathrm{K-PINN}}](\mathrm{c}_{\mathrm{j}},\omega)\parallel^{2} \tag{20}$$

Finally, the total loss function is written as:

$$\mathcal{L}(\theta)=\lambda_{\mathrm{f}}\mathcal{L}_{\mathrm{f}}^{\mathrm{w}}(\theta)+\lambda_{\mathrm{p}}\mathcal{L}_{\mathrm{p}}^{\mathrm{w}}(\theta)+\lambda_{\mathrm{r}}\mathcal{L}_{\mathrm{reg}}(\theta). \tag{21}$$

This design enables synchronous spatial adjustment of the supervised information and the physical constraints. In highly uncertain regions such as the leading edge near the blade tip, both the supervised and physical-residual weights are increased, thereby encouraging the residual network to focus on correcting the prior deviation. In low-uncertainty regions such as the trailing edge of the blade body, the weights are reduced, allowing the model to inherit more of the smooth trend from the statistical prior and reducing the risk of overfitting. Figure 2 shows the architecture diagram of the Kriging information-augmented physical neural network in this paper.

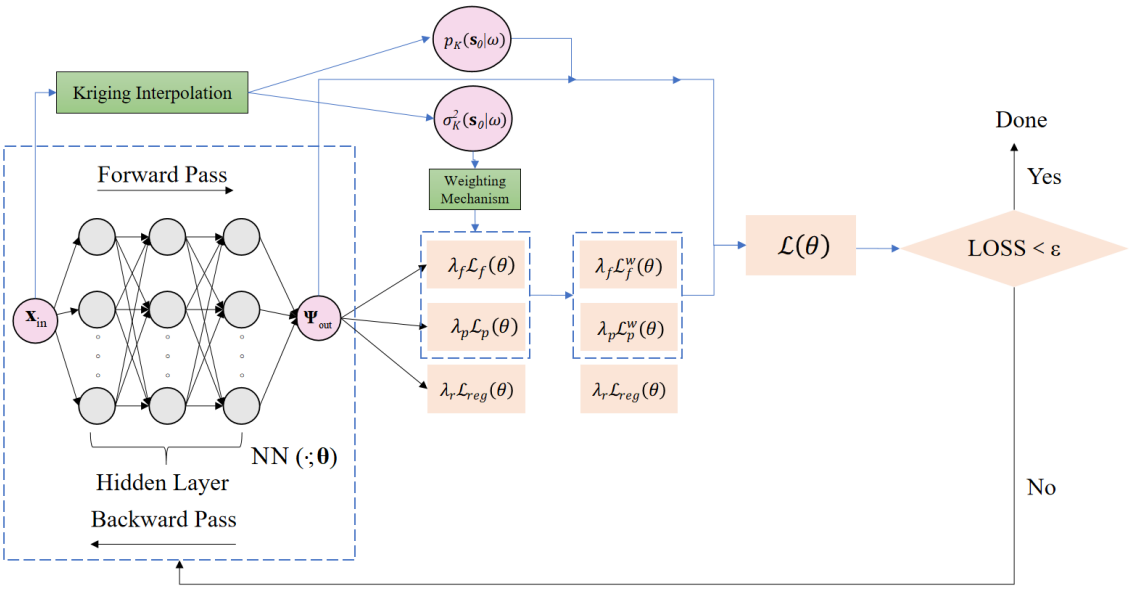

Figure 2. Architecture diagram of the Kriging information-augmented physical neural network (K-PINN).

3. Experiment

3.1. Blade region division and measurement point positioning

The research object of this paper is the pressure distribution on the upper surface of a rotor blade. The total blade length is L = 58.2 cm, and the maximum chord length is C_{max} = 9.2 cm. Considering the significant interference caused by the mounting structure and hub at the blade root, as well as the limitations in the arrangement and attachment of flexible sensors in this region, a 6.0 cm segment at the blade root mounting area is excluded from both modeling and result evaluation. Consequently, the effective spanwise length is L_e = 52.2 cm.

A Cartesian coordinate system is established on the upper surface of the blade, with the lower-left corner of the effective measurement region defined as the coordinate origin. The sampling points of the flexible pressure sensor array are regularly distributed in a discrete manner with a uniform spacing of 0.3 cm determined by the sensor layout density. The mesh contains 175 nodes in the chordwise direction and 32 nodes in the spanwise direction.

To exclude invalid regions outside the blade from training and error evaluation, an external rectangular mesh combined with a geometric mask is adopted to define the effective computational domain. The mask value is set to 1 if a grid point lies within the blade contour and inside the valid spanwise range; otherwise, the mask value is set to 0.

To support the layout of key measurement points, sensitivity analysis of missing regions and zonal error statistics, the effective measurement region is divided in both the spanwise and chordwise directions (as shown in Figure 3), and combined subregions are further defined on this basis.

For the effective spanwise length L_e, a dimensionless spanwise coordinate is defined as $\eta = x/L_e \in [0,1]$. According to the proportion of the effective spanwise length, the measurement domain is divided into three spanwise segments:

(1) Blade root region: $\eta \in [0,0.15]$; (2) Blade body region: $\eta \in (0.15,0.85]$; (3) Blade tip region: $\eta \in (0.85,1]$.

In the chordwise direction, a dimensionless chordwise coordinate $\xi \in [0,1]$ is adopted to be consistent with the coordinate definition (where 1 denotes the trailing edge and 0 denotes the leading edge), and the chordwise domain is bisected into two parts:

(4) Trailing edge region: $\xi \in (0.5,1]$; (5) Leading edge region: $\xi \in [0,0.5]$.

Only a small number of discrete pressure measurement points are generally available under engineering constraints. In this paper, 15 key measurement points are selected as sparse inputs to reconstruct the full-field pressure distribution within the effective measurement region.

A hierarchical point layout scheme with 5 representative spanwise cross-sections and 3 representative chordwise positions is adopted in this study, resulting in a total of 15 sparse measurement points as shown in the figure. The representative spanwise cross-sections are selected at the center of the blade root region, the inner/middle/outer segments of the blade body, and the center of the blade tip region, so as to cover the structural variations of the root, body and tip regions. The chordwise positions are chosen at representative points near the trailing edge, the mid-chord, and the leading edge, to constrain both the pressure recovery and the leading edge peak characteristics simultaneously.

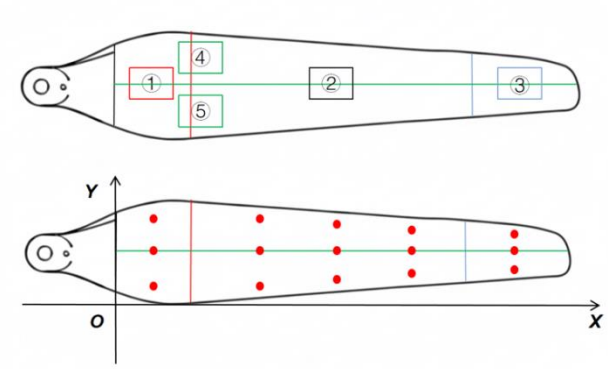

Figure 3. Rotor surface zoning and sparse point distribution.

3.2. Experimental platform construction

An experimental system for measuring blade surface pressure, as illustrated in Figure 4, is developed in this study. To address the challenge of signal lead-out from rotating components, a high-speed slip ring is employed for signal transmission. A customized structure is adopted for the main shaft of the rotor motor, with a through-hole of approximately 5 mm in diameter machined at the shaft center. The leads of the sensor array are routed through the blade and the internal bore of the main shaft, and then connected to the high-speed slip ring module. This slip ring is equipped with 12 channels and can operate stably at a maximum rotational speed of 600 rpm, enabling lossless transmission of analog and digital signals from the rotating side to the stationary side and thus ensuring the continuity and reliability of data acquisition.

The structure of the scaled rotor test rig, as shown in the figure, consists of a G10-10KGF dynamometer test stand, a slip ring-integrated motor, custom-matched rotor blades, and an electronic speed controller.

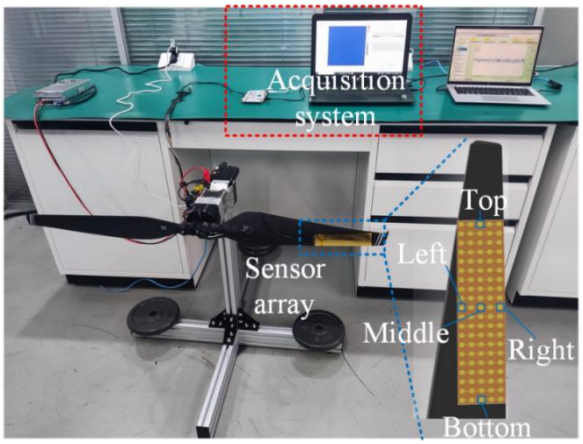

Figure 4. Blade pressure measurement system and sensor installation.

3.3. Dataset construction

To support the subsequent research on full-field pressure reconstruction of rotor blades based on K-PINN, full-coverage pressure acquisition was carried out at a step of 5 rpm within the rotational speed range of 90–600 rpm, yielding full-field pressure data covering a wide operating condition range. The flexible sensor array covers the effective measurement region of the blade, and approximately 3000 valid discrete

measurement points can be obtained under each rotational speed condition (after excluding points outside the blade profile, the excluded mounting region and defective points). This forms supervised data corresponding to operating condition parameters (rotational speed), spatial coordinates and pressure values, providing a data foundation for the model to learn the spatial pressure distribution structure and its variation law with rotational speed.

A total of 103 groups of valid rotational speed condition data were actually collected in this study, and a mean pressure field was constructed for each rotational speed condition as the final sample. Thus, the sample size of the dataset in this study is on the order of 10^2 ; each sample contains approximately 3000 valid spatial discrete points, and the overall scale of valid data points reaches approximately 3×10^5. This dataset features both wide coverage of operating conditions and dense spatial sampling under a single condition. It can not only support the model to learn the variation law of the overall pressure field morphology at different rotational speeds but also provide sufficient spatial constraints and evaluation benchmarks for continuous modeling based on coordinate input.

Combined with the sampling frequency and steady-state statistical strategy adopted in this study, lightweight filtering combined with steady-state statistics was used in the preprocessing stage to suppress random noise and isolated burrs. Median filtering was performed on the time-series signals of each channel to weaken single-frame spikes, and then the mean field was calculated within the steady-state window to further reduce the influence of random noise on the spatial distribution.

To verify the reliability of the collected data, the output of the sensor unit in the central area of the array was quantitatively compared with that of a commercial pressure sensor (S18-100k) at the same position. The results show a high consistency in the signal trends of the two, which can serve as direct evidence for the accuracy and reliability of the measurement system. Table 2 shows the comparison between the data collected by the selected sensor and the commercial sensor data in this paper.

Table 2. Comparison with commercial sensor data.

Index Name	Value	Unit
MSE	7.43×10^{-4}	kPa^2
RMSE	0.0273	kPa
MAE	0.0211	kPa
R^2	0.987	/

3.4. Model training

The training process is organized as a two-level sampling scheme consisting of operating-condition batches and spatial patches. At the outer level, mini-batches are constructed on a per-condition basis; at the inner level, the valid measurement domain is partitioned and sampled within each condition.

A total of approximately 103 operating conditions were obtained in the experiments. For each condition, the sensor array covers the valid measurement domain of the blade, and the full-field discretized point set contains about 3000 points for a single condition. The acquisition frequency is 10 Hz, and 10 s of data are collected for each condition. After the rotational speed reaches a stable state, a steady-state time window is selected and statistically averaged, thereby yielding one steady-state mean pressure-field sample for each operating condition. Therefore, the basic sample unit used for K-PINN training is one mean field corresponding to one rotational-speed condition. The total number of samples

used here is about 77, and the corresponding 15-point sparse input is extracted from the mean field at fixed spatial positions.

3.4.1. Network structure, input-output configuration, and residual learning implementation

A sparse observation encoder combined with a coordinate decoder architecture is adopted. For each operating condition, the pressure values at the 15 sparse sampling points are assembled into a vector $z(\omega)$ which is concatenated with the normalized rotational speed and then fed into the encoder. The encoder adopts a three-layer fully connected multilayer perceptron (MLP) with layer widths of 64, 64, and 32, respectively, and the tanh activation function is employed. Subsequently, the decoder takes the query coordinates and operating condition features $(\tilde{x}, \tilde{y} \mid \omega)$ and $z(\omega)$ as inputs, and outputs the residual correction term $\Delta p_\theta(\tilde{x}, \tilde{y}, \omega)$. The decoder is a six-layer MLP with width 128 for each layer (128×6), where the hidden layers also use tanh and the output layer is linear. The final pressure prediction is represented in residual-composition form:

$$p_{K-PINN}(\tilde{x}, \tilde{y} \mid \omega) = p_K(\tilde{x}, \tilde{y} \mid \omega) + \Delta p_\theta(\tilde{x}, \tilde{y}, \omega) \tag{22}$$

where p_K denotes the Kriging prior mean field. This structure allows the network to primarily learn the deviation of the prior rather than fit the entire field from scratch, thereby promoting more stable convergence under the 15-point input condition and concentrating the correction on regions where the prior is unreliable.

To improve training stability, linear normalization is applied to both the input coordinates and rotational speed in this study: the coordinates $(\tilde{x}, \tilde{y})$ are mapped to $[-1,1]$, and the rotational speed ω is scaled to $[0,1]$. Pressure values are standardized using the mean and standard deviation within each operating condition. The network output Δp_θ is learned in the standardized feature space, and inverse normalization is finally performed to obtain pressure predictions in units of kPa.

3.4.2. Sampling of supervision points and collocation points

Each operating condition corresponds to a full-field steady mean pressure full-field reference data, containing approximately 3000 original discrete points. To ensure full spatial coverage while controlling the computational cost per iteration, random subsampling is performed on the supervised point set Ω_N in each training epoch. A total of $N_s = 1200$ points are sampled to construct the supervised subset Ω_{N_s}, which is adopted to calculate the weighted supervised loss $\mathcal{L}_f^w$. This sampling size accounts for about 40% of the total full-field points per operating condition, enabling stable constraints on the major spatial flow structures with affordable numerical cost.

The physical residual term is calculated over a set of collocation points C. In this study, $N_c = 2000$ collocation points are sampled per epoch for each operating condition, adopting a strategy combining global uniform sampling with refined sampling in sensitive regions. The collocation points are allocated according to the following proportions: 50% for the global domain, 20% for the leading-edge half-chord region, 20% for the blade tip region, and 10% for the coupled sensitive region of the blade tip and leading edge. This design ensures the global continuity constraints are fully retained, while increasing the constraint density in regions prone to extrapolation errors. Accordingly, the physical residual can effectively suppress local oscillations and numerical drift within sensitive areas.

Furthermore, to mitigate extrapolation artifacts near the mask boundary, an additional $N_h = 200$ boundary points are sampled on $\partial\Omega$, and a weak boundary term enforcing zero normal gradient is introduced. The weighting coefficient of the boundary term is set to $\beta_b = 0.1$, which guarantees boundary stability without introducing excessive smoothing that distorts internal flow structures.

3.4.3. Definition of a batch

In this paper, a mini-batch is defined as a set of mean-field samples containing $B_\omega = 8$ distinct operating conditions. For each operating condition within a batch, $N_s = 1200$ supervised points, $N_c = 2000$ collocation points, and Nb = 200 boundary points are sampled. The supervised loss and physical residual loss are calculated under the same weight configuration.

Therefore, in each training iteration (*i.e.*, one parameter update), the actual amount of data participating in the loss computation is approximately:

$$N_{data/step} = B_\omega \cdot N_s = 8 \times 1200 = 9600,$$

$$N_{phys/step} = B_\omega \cdot N_c = 8 \times 2000 = 16000,$$

and the number of boundary points is $8 \times 200 = 1600$. Under controllable computational cost, this setting ensures that each iteration contains sufficient full-field supervision information and extrapolation-stability constraints, while allowing the patch-enhancement strategy to allocate more collocation points to sensitive regions such as the blade-tip leading edge.

3.4.4. Training strategy

A two-stage optimization strategy is adopted in this study: in Stage I, the Adam optimizer is used for rapid convergence; in Stage II, the optimization is switched to L-BFGS for fine fitting, so as to further reduce the physical residual and improve local structural consistency. At the early stage of training, the total loss decreases rapidly. It then enters a long interval of slow decrease with fluctuations. A clear secondary decrease appears near 2.0×10^4 iterations, indicating that training enters the refinement stage. Figure 5 illustrates the loss function trend during the model training process in this paper.

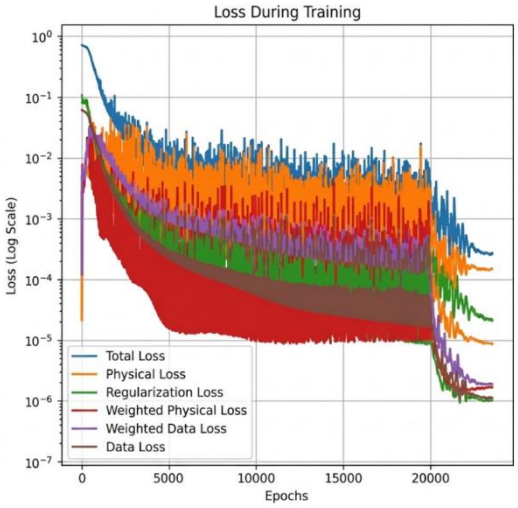

Figure 5. Trend of the loss function during training.

(1) Stage I: Main Adam Training

At the early stage, the Adam optimizer is used to obtain a stable global convergence trend. The initial learning rate is set to 1×10^{-3}, and a stepwise decay schedule is adopted: at the 5000th, 12,000th, and 18,000th iterations, the learning rate is multiplied by 0.5, *i.e.*, $10^{-3} \rightarrow 5 \times 10^{-4} \rightarrow 2.5 \times 10^{-4} \rightarrow 1.25 \times 10^{-4}$. This allows the optimization process to gradually transition from rapid descent to stable refinement. This setting corresponds to the continuous decline of the total loss over the 0–20,000 iteration interval, while also allowing reasonable fluctuations induced by mini-batches and random point sampling.

To coordinate with the spatial-weighting strategy described in Section 2.3, a progressive schedule is also applied to the weighting strength and the physical-loss coefficient. During the first 6000 iterations, a weaker weighting strength $\alpha=1$ and a smaller physical-loss coefficient $\lambda p = 0.1$ are used to ensure that the model first obtains a globally stable solution. Then, during iterations 6000–20,000, α is linearly increased to 3 and λ_p is increased to 0.8, so that the training focus gradually shifts toward correction in high-uncertainty regions. The residual-regularization weight is set to $\lambda r = 5 \times 10^{-3}$ to constrain the magnitude of Δp_θ and avoid excessive disturbance in regions where the prior is reliable.

(2) Stage II: Refinement Stage

Once training enters the region around 20,000 iterations, all loss components exhibit a simultaneous rapid decrease, indicating that the model has entered the neighborhood of a feasible solution and is suitable for stronger refinement optimization. In this stage, a refinement strategy is adopted in which the learning rate is further reduced to 5×10^{-5} and kept fixed, in order to significantly reduce both the data term and the physical residual while improving local consistency. The secondary decrease near 20,000 iterations corresponds to this stage, where the global morphology is already largely stable and the model can reduce the supervised error and physical residual simultaneously under a smaller step size, thereby obtaining a more consistent full-field solution.

3.4.5. Stopping criterion and validation monitoring

Training is stopped when the validation loss shows no significant decrease for 200 consecutive epochs, and the model parameters are rolled back to those corresponding to the minimum validation loss. The low-speed extrapolation interval (90–145 r/min), the high-speed extrapolation interval (555–600 r/min), and the held-out intermediate rotational speeds (200, 300, 400, and 500 r/min) are used as extrapolation-evaluation sets and do not participate in model training. The remaining conditions are used for training and validation, with the validation set consisting of approximately 10% of the rotational-speed levels drawn at uniform intervals from the training conditions.

3.4.6. Model training parameters

Table 3 lists part of the hyperparameters of the model in this paper.

Table 3. Network architecture and hyperparameters.

Category	Parameter	Value
Input/Output	Number of sparse input points	15
	Operating condition parameters	ω (normalized to [0,1])
	Residual form	$p_{K\text{-}PINN} = p_K + \Delta p_\theta$
Data Scale	Number of operating condition samples	$N_w \approx 103$
	Full-field point number per operating condition	Approximately 3000
Encoder	Number of layers	3 layers：64–64–32 (tanh)
	Output dimension	32
Decoder	Number of layers	6 layers：128 × 6 (tanh)
Sampling	Supervised subsampling	N_s = 1200per operating condition per step
	Number of collocation points	N_c = 2000per operating condition per step
	Number of boundary points	N_b = 200per operating condition per step
	Patch ratio	Global domain 50%/Leading edge 20%/ Blade tip 20%/Coupled region 10%
Batch	Number of operating conditions	$B_\omega = 8$
Optimization	Stage I (Adam) iterations	0–20,000
	Adam learning rate	$10^{-3} \rightarrow 5 \times 10^{-4} \rightarrow 2.5 \times 10^{-4} \rightarrow 1.25 \times 10^{-4}$
	Stage II iterations	20,000–24,000
	Refinement learning rate	5×10^{-5}
Loss Weight	λ_f	1.0
	λ_p	0.1（≤ 6k） → 0.8（gradually increased up to 20k）
	λ_r	5^{-3}
	β_b	0.1
	ε	1×10^{-6}
Spatial Weighting	w_{min}, w_{max}	1.0,4.0
	α	1（≤ 6k） → 3（linearly increased up to 20k）

3.4.7. Computational cost and inference efficiency

For the proposed K-PINN model, the main computational burden is concentrated in the offline training stage, whereas the online deployment stage allows relatively fast computation. Overall, the framework is more naturally organized as an offline-training plus online-inference paradigm.

It should be emphasized that the present study does not train an independent model for each rotational-speed condition. Instead, a unified model is constructed using multi-speed operating-condition samples, with the rotational-speed parameter included as part of the input. Therefore, the training cost reported here corresponds to one unified multi-condition model, rather than to a separate training process for a single speed condition. This unified model is built on approximately 103 operating-condition samples, each corresponding to one steady-state mean pressure field and containing about 3000 valid discrete points.

The experimental environment was equipped with an Intel i7-12700KF processor, an RTX 3080 GPU with 10 GB memory, and a PyTorch-based software environment. Under the current training scale and optimization setting, the total wall-clock time for one complete training run was 3.75 h. Among this, the Adam-based main training stage accounted for about 70% of the total training time, corresponding to 2.63 h, whereas the late-stage refinement accounted for about 30%, corresponding to 1.12 h. In terms of convergence efficiency, the model can be regarded as entering a stable convergence regime near 2.15×10^4 iterations, after which the rate of loss reduction becomes significantly smaller and the training focus gradually shifts toward local structural consistency and residual refinement.

Compared with the offline training stage, the computational burden of K-PINN during testing is significantly lower. For a single test case, the model only requires the 15 sparse pressure measurements, the normalized rotational-speed parameter, and the query coordinates to reconstruct the full-field pressure distribution. Since no parameter update is involved during inference, the computation is mainly determined by the scale of the network forward pass and the number of query points. The average inference time required to reconstruct one full-field pressure map for a single test case was 2.3 s/case, indicating acceptable efficiency.

In summary, the proposed method does incur a certain offline computational cost during training, whereas the inference-stage cost remains low enough to support rapid full-field reconstruction. Compared with a purely data-driven method, the additional training cost introduced by K-PINN mainly comes from the evaluation of the physical residual, spatial weighting, and the two-stage optimization procedure. In return, the model achieves improved stability and robustness in high-uncertainty regions, extrapolation conditions, and critical-structure preservation (as discussed in the following sections). Therefore, the adopted offline-training plus online-inference workflow is consistent with the engineering positioning of the present rotor pressure-field reconstruction task.

3.5. Generalization and ablation experiments

3.5.1. Generalization experiment

To verify the reconstruction stability and generalization capability of the proposed K-PINN under unseen operating conditions, this section conducts systematic tests under two types of scenarios: interval extrapolation and discrete held-out rotational-speed conditions. According to the rotational-speed coverage range and data-acquisition strategy adopted in this study, three test sets are constructed, none of which participate in model training:

(1) LOSO test set: four discrete rotational-speed points, namely ω = 200, 300, 400, and 500 r/min, are held out and used only for testing, in order to evaluate interpolation-type generalization within the training interval.

(2) Low-speed extrapolation test set: $\omega \in [90, 145]$ r/min is selected as the low-speed extrapolation interval to evaluate extrapolation stability at the low-speed end.

(3) High-speed extrapolation test set: $\omega \in [555, 600]$ r/min is selected as the high-speed extrapolation interval to evaluate extrapolation stability at the high-speed end.

3.5.2. Ablation experiment

In addition, in order to verify the actual contributions of the spatially adaptive weighting mechanism based on the Kriging uncertainty map and the physical constraints to reconstruction performance, ablation experiments are further carried out in this section. Two groups of comparison models are established, with only one factor changed in each group and all other training settings kept identical, so that the difference can be mainly attributed to the weighting strategy and the constraints themselves:

(1) A purely data-driven model (without physical constraints).

(2) A model without uncertainty-based spatially adaptive weighting, *i.e.*, the weight field generated through the mapping function is removed.

3.6. Layout sensitivity analysis

To quantify which sparse measurement points in specific regions are more critical to the full-field reconstruction accuracy under the constraint of a limited number of points, a zonal perturbation experiment is proposed. With the model structure, parameters and test conditions kept unchanged, strong perturbations (100% noise) are only introduced to the sparse measurement points at the input end, and the degradation amplitude of the global error index is observed. This experiment establishes a direct correlation between the model error characteristics and the spatial information contribution, thus providing a quantitative basis and engineering interpretation for the priority of measurement point layout.

Four regions are selected herein: the blade tip region, blade body region, leading edge region and trailing edge region. In each experiment, only the sparse points within one of these regions are perturbed, while the points in the other regions remain unchanged.

Considering the differences in the pressure amplitude magnitude and fluctuation scale across different regions, direct multiplicative perturbation on the original pressure values would result in incomparable noise energy across regions. For this reason, 100% noise is defined herein as the perturbation intensity relative to the intrinsic scale of the input signal in the target region. Zero-mean noise η_i is added to the pressure $\tilde{p}_i$ of the measurement points in the region, and the noise standard deviation is calibrated using the regional scale

$$s_Z{:}\tilde{\mathrm{p}}_\mathrm{i} = \bar{\mathrm{p}}_\mathrm{i} + \eta_\mathrm{i}, \quad \eta_\mathrm{i} \sim \mathcal{N}(0, \sigma_Z^2), \quad \sigma_Z = \alpha s_Z, \alpha = 1.0 \tag{23}$$

where s_Z is taken as the standard deviation of the pressure at the sparse points in the region, ensuring that the 100% perturbation in different regions has a consistent meaning of relative intensity.

Since the four regions contain different numbers of sparse points, perturbing all points in a region would naturally inject more noise sources into regions with a larger number of points, leading to the mixing of the point number effect into the sensitivity evaluation. To ensure comparability, a two-step processing method is adopted in this study:

(1) Perturbation energy normalization: On the basis of regional scale calibration, the noise amplitude is scaled according to the number of points in the region (3 points are taken herein), so that the total perturbation energy injected into different regions is consistent.

(2) Equal-point perturbation: Fix the number of perturbed points to 3 in each experiment (*i.e.*, the minimum number of points among the four regions). 3 points are randomly sampled within the target region, the experiment is repeated multiple times, and the mean value and fluctuation range are statistically analyzed.

4. Results and discussion

4.1. Generation of Kriging prior field and uncertainty map

4.1.1. Global reconstruction performance of the prior field

Figure 6 presents the prior mean field generated from 15 sparse measurement points under the representative operating condition of 285 rpm. Overall, the output of global Kriging is continuous and smooth within the effective domain, and is capable of reproducing the macroscopic distribution trends of the pressure field (e.g., the overall gradient direction), which fulfills the positioning of the steady statistical prior

in this chapter. The morphology of the prior mean field is jointly determined by observational constraints and spatial correlation structures. In regions with more prominent high-gradient and non-stationary characteristics such as the leading-edge suction peak and blade tip, the global single-scale correlation structure tends to introduce a certain degree of smoothing, making it difficult to fully reconstruct the morphology of local extreme values by relying solely on the statistical prior. The objective of this chapter is to provide a usable full-field initial solution, and this is not regarded as a defect in this study; instead, the fine correction of key complex regions will be implemented in subsequent work.

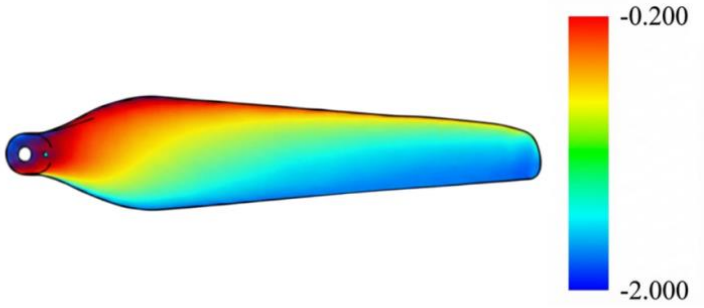

Figure 6. Results of Kriging prior field at 285 rpm.

4.1.2. Uncertainty map generation

Figure 7 shows the prediction variance $\sigma_K^2(\tilde{x}, \tilde{y})$ output synchronously with the prior mean field under the operating condition of 285 rpm. This variance is mainly determined by the geometric distribution of measurement points and the correlation structure, and is regarded as a spatial uncertainty characterization of the prior prediction. Combined with the fixed 15-point layout adopted in this study, the uncertainty map typically exhibits high values in regions far from the measurement points, near the boundaries, and in complex regions such as the blade tip and leading edge.

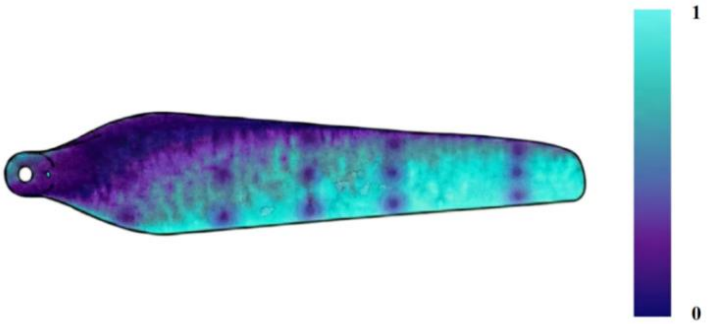

Figure 7. Normalized uncertainty map.

4.1.3. Kriging result analysis

To quantitatively evaluate the relative confidence capability of σ_K^2, the Spearman rank correlation coefficient and Top-q% risk capture rate are adopted as evaluation metrics. Metrics are presented from both the global and zonal perspectives, with a focus on examining their performance in ranking and capturing high-error regions. Table 4 shows the zonal statistical results.

Table 4. Zonal statistics of prior errors and uncertainties.

Zonal	RMSE (kPa)	MAE (kPa)	R^2	$\rho(\sigma\_K^2,\|e\|)$	Proportion of Top-20% Error Energy (%)
Global	0.21	0.19	0.81	0.58	56
Blade Tip Region	0.27	0.22	0.71	0.66	62
Blade Body Region	0.19	0.14	0.83	0.52	50
Blade Root Region	0.20	0.19	0.79	0.57	54
Leading-Edge Half Chord	0.22	0.15	0.82	0.63	60
Trailing-Edge Half Chord	0.18	0.09	0.89	0.46	47
Blade Tip Leading Edge	0.34	0.25	0.70	0.71	70
Blade Tip Trailing Edge	0.20	0.13	0.83	0.55	52
Blade Root Leading Edge	0.24	0.16	0.78	0.62	58
Blade Root Trailing Edge	0.18	0.11	0.80	0.48	46

From the visualization results of the representative operating condition, the prior mean field maintains good continuity and rationality of the overall distribution within the effective measurement domain, and can reflect the macroscopic gradient direction of the pressure field and the positions of major low-pressure regions under negative pressure-dominated conditions. Meanwhile, the uncertainty map exhibits an obvious spatially inhomogeneous distribution characteristic.

Based on the global statistical results, the error level between the prior mean field and the full-field reference data mean field is within an acceptable range, with a global RMSE of 0.21 kPa, MAE of 0.19 kPa and a correlation coefficient of 0.81. This result indicates that global Kriging can effectively recover the macroscopic spatial distribution of the pressure mean field.

In the spanwise division, the blade body region achieves the best performance (RMSE = 0.19 kPa, $R^2 = 0.83$), followed by the blade root region (RMSE = 0.20 kPa, $R^2 = 0.79$), while the blade tip region has the largest error (RMSE = 0.27 kPa, $R^2 = 0.71$). This phenomenon is consistent with the engineering consensus that the blade tip region has stronger three-dimensional effects, shorter local scales and more prominent non-stationarity, where smoothing and local deviations are more likely to occur.

In the chordwise division, the error in the leading-edge half chord is significantly higher than that in the trailing-edge half chord (leading edge: RMSE = 0.22 kPa, $R^2 = 0.82$; trailing edge: RMSE = 0.19 kPa, $R^2 = 0.89$). This demonstrates that due to the steeper pressure gradient and more drastic local variations in the leading-edge region, global Kriging alone cannot fully preserve the local structures under sparse constraints, thus leading to a higher tendency of deviations. In contrast, the trailing-edge region undergoes more gentle overall variations, enabling the stable reconstruction of the prior field with greater ease.

The above results indicate that the main sources of error in the global Kriging prior can be attributed to the overlapping regions of the tip effect and the high-gradient leading edge, and this conclusion also provides a direct basis for identifying the key regions to be corrected in the subsequent K-PINN model.

4.2. K-PINN reconstruction results

After the completion of model training, the physics-informed neural network is used for field reconstruction. The model performance is evaluated from both quantitative and qualitative dimensions by comparing the reconstruction results with the known full-field reference data solutions.

Rotational speeds of 120 rpm, 285 rpm and 580 rpm are selected as representative operating conditions to conduct quantitative evaluation and visual verification on the steady mean pressure field on the blade surface reconstructed by K-PINN. For these operating conditions, the model takes the mean pressure values of the fixed 15 sparse measurement points as input, and outputs the full-field mean pressure prediction over the effective measurement domain of the blade. The evaluation is based on the full-field reference data mean pressure, with a focus on examining the consistency of the overall amplitude, the consistency of the spatial distribution, and the local error level in sensitive regions. Figures 8 to 10 present the full-field comparison results of the model-predicted pressure fields under the three typical operating conditions. In terms of the overall morphology, the predicted field can well reproduce the dominant characteristics of the negative pressure distribution. The entire upper surface of the blade is subject to negative pressure, where the negative pressure level gradually decreases from the leading edge to the trailing edge along the chordwise direction; along the spanwise direction, the blade tip region exhibits more intense spatial gradient variations due to the tip effect.

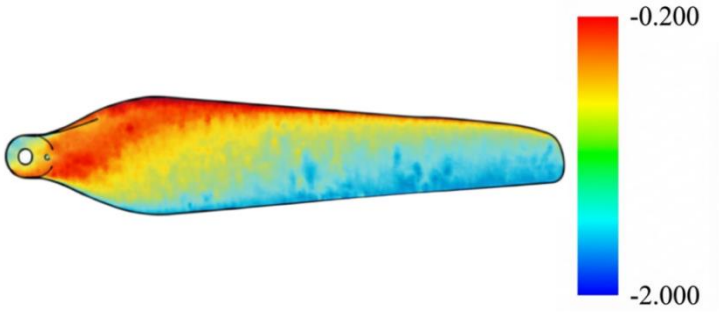

Figure 8. K-PINN reconstruction results at 120 rpm operating condition.

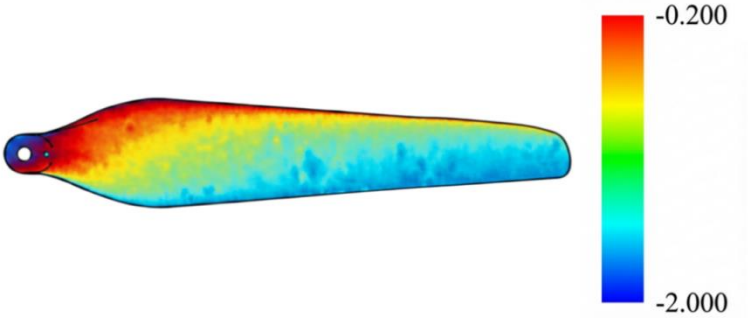

Figure 9. K-PINN reconstruction results at 285 rpm operating condition.

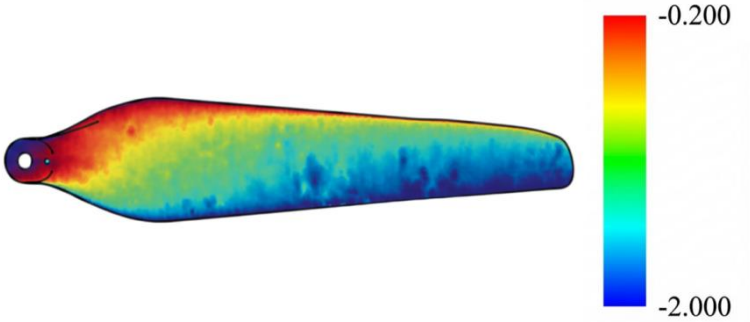

Figure 10. K-PINN reconstruction results at 580 rpm operating condition.

For further quantitative evaluation, Table 5 summarizes the zonal statistical results of reconstruction errors for the K-PINN model.

In the result verification of representative operating conditions, the reconstruction results of K-PINN were evaluated both quantitatively and qualitatively by taking the 285 rpm operating condition as an example. The results show that this method can achieve a relative error level of approximately 4% over the global domain and can well preserve the overall structural characteristics of the pressure field. Errors are mainly concentrated in high-gradient regions such as the blade tip leading edge, which verifies the rationality of the integrated framework combining statistical prior, uncertainty weighting and physical constraints.

Table 5. Quantitative comparison of PINN prediction against full-field reference data.

Zonal	RMSE (kPa)	MAE (kPa)	Relative Error (%)
Global	0.10	0.07	4.0
Blade Tip Region	0.14	0.10	5.6
Blade Body Region	0.08	0.06	3.2
Blade Root Region	0.11	0.08	4.4
Leading-Edge Half Chord	0.13	0.09	5.2
Trailing-Edge Half Chord	0.07	0.05	2.8
Blade Tip Leading Edge	0.18	0.13	7.2
Blade Tip Trailing Edge	0.11	0.08	4.4
Blade Root Leading Edge	0.14	0.10	5.6
Blade Root Trailing Edge	0.08	0.06	3.2

4.3. Generalization performance analysis

A representative operating condition is selected from each of the three test sets (100 rpm, 300 rpm, and 600 rpm), and the reconstructed prediction fields are presented. In addition, full-domain errors are statistically summarized for the generalization test sets. Figure 11 presents the reconstruction results under three typical working conditions in this paper.

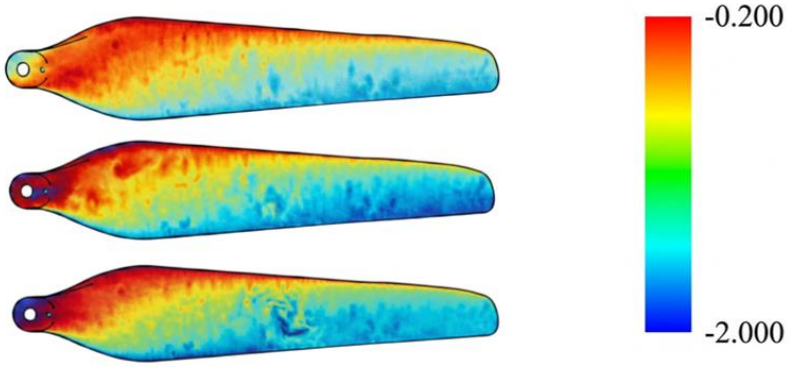

Figure 11. The reconstruction results of the generalization experiment are presented for 100 rpm, 300 rpm, and 600 rpm from top to bottom.

Table 6 summarizes the full-domain error statistics of the three test sets. It can be seen that the model performs best on the LOSO test set, with a full-domain relative error of 3.6%. The full-domain relative error for low-speed extrapolation is 4.2%, and the error further increases to 4.7% for high-speed extrapolation. These results indicate that the model is able to learn the main mapping law across different rotational speeds. Although the extrapolation errors at both ends increase, with the increase being more evident at the high-speed end, the overall error remains controllable, demonstrating that the model possesses a certain interval-transfer capability. The spatial sources of the errors are consistent: generalization remains relatively stable in smooth regions such as the trailing edge of the blade body, whereas the most significant error amplification under extrapolation conditions appears in sensitive regions such as the leading edge near the blade tip. Figure 12 shows the results of the ablation experiments in this paper.

Table 6. Summary of full-domain error statistics for the generalization test sets.

Test set	Number of cases	RMSE (kPa)	MAE (kPa)	Relative error (%)
LOSO	4	0.090	0.064	3.6
Low-speed extrapolation	12	0.105	0.075	4.2
High-speed extrapolation	10	0.118	0.085	4.7

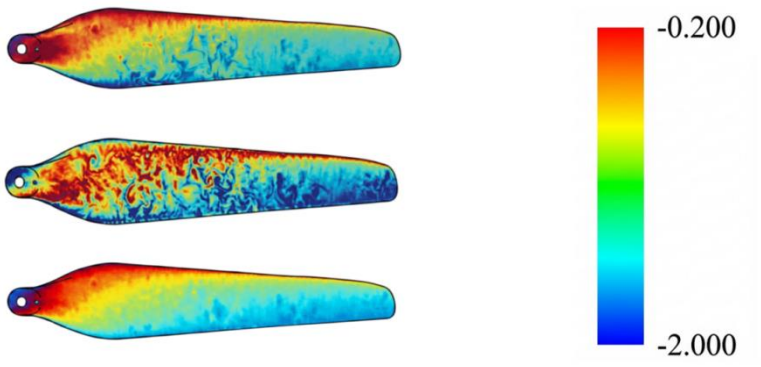

Figure 12. Comparison of reconstruction results of different models under the same operating condition (285 rpm). from top to bottom: the model without uncertainty-based spatially adaptive weighting, the purely data-driven model, and the K-PINN model.

Table 7 gives the comparison of full-domain errors of the two models on the test set. It can be seen that the purely data-driven baseline model yields a full-domain relative error of about 35.0%, whereas the model without uncertainty-based spatially adaptive weighting reduces the full-domain relative error to about 18.2%. These results indicate that, for the present reconstruction task from sparse input to full-field output, the main bottleneck in training performance is not determined solely by network capacity or sample size. Instead, the spatial allocation in the loss function plays a decisive role in the optimization trajectory and in the quality of the converged solution.

Table 7. Comparison of full-domain errors for the two ablation models.

Model	RMSE (kPa)	MAE (kPa)	Relative error (%)
Purely data-driven	0.830	0.610	35.0
Without spatially adaptive weighting	0.432	0.318	18.2

4.4. Results of sensitivity analysis on measurement point layout

Figure 13 and Table 8 present the comparison of global reconstruction results and error levels for the baseline model and after zonal perturbations in four types of regions. The global accuracy of the baseline model on the test set is as follows: RMSE = 0.10 kPa, MAE = 0.07 kPa, and relative error = 4.0%. After introducing perturbations to the sparse inputs of different regions respectively, the global relative error increases significantly with distinct disparities observed. Perturbations to the blade tip and leading edge both lead to a relative error of approximately 22%, the highest among the four types; the perturbation to the trailing edge results in a relative error of about 16%, and that to the blade body around 14%. These results indicate that the sparse input information from the leading edge and blade tip regions exerts the strongest constraint on the model output. Once such information is contaminated by strong noise, the overall error level of the model will increase remarkably.

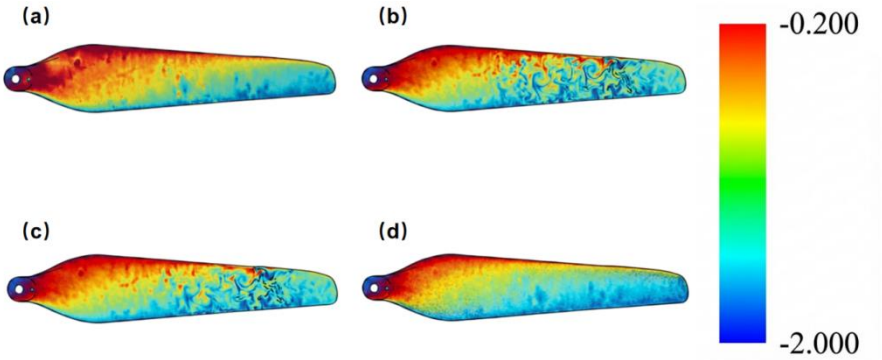

Figure 13. Reconstruction results of zonal perturbations: **(a)** trailing-edge region perturbation; **(b)** leading-edge region perturbation; **(c)** blade tip region perturbation; **(d)** blade body region perturbation.

Table 8. Comparison of global error levels in zonal perturbation experiments.

Zonal	RMSE (kPa)	MAE (kPa)	Relative Error (%)
Baseline (No Perturbation)	0.10	0.07	4.0
Blade Tip Region Perturbation	0.55	0.38	22.8
Blade Body Region Perturbation	0.35	0.24	14.2
Leading-Edge Region Perturbation	0.55	0.38	22.2
Trailing-Edge Region Perturbation	0.40	0.28	16.3

5. Conclusions

Focusing on the core problem of non-destructive acquisition and sparse reconstruction of the pressure field on the blade surface under rotating conditions, this paper constructs an integrated research framework encompassing flexible array measurement, statistical prior extrapolation, physics-constrained reconstruction, model generalization experiments, and layout sensitivity analysis. The effectiveness of the scheme of flexible sensing array measurement + Kriging prior + PINN reconstruction in rotor pressure field reconstruction is successfully verified. The K-PINN model exhibits excellent reconstruction performance with a reconstruction error as low as 4%, and accurately captures key aerodynamic features such as the leading-edge suction peak simultaneously. This innovative method effectively overcomes the inherent limitations of traditional technologies, including aerodynamic shape

damage, sparse measurement points, and the lack of physical constraints, providing a robust and reliable solution for the high-precision acquisition of rotor system pressure fields.

In terms of generalization capability, the relative errors for in-interval interpolation and extrapolation beyond both boundaries reach 3.6%, 4.2%, and 4.7%, respectively, demonstrating the model possesses favorable generalization performance across parameter ranges. Comparative experiments between the purely data-driven model and the version without spatial weighting reveal a significant increase in prediction error, which verifies that relying solely on supervised fitting is insufficient to obtain a robust solution. Meanwhile, through zonal missing sensitivity analysis, the impacts of sparse point information in different regions on reconstruction accuracy are quantitatively compared, thereby providing a basis and explanation for the priority of measurement point layout under the condition of limited point numbers. It should also be noted that the present validation scenarios remain relatively controlled, and the current study mainly focuses on steady mean pressure-field reconstruction. More systematic robustness evaluations under synthetic measurement noise, further sensor reduction, and dynamic operating conditions are therefore still needed and are left for future work.

Data availability statement

The experimental data may involve sensitive information and thus cannot be made publicly available for confidentiality reasons.

Declaration of generative AI and AI-assisted technologies

During the preparation of this manuscript, the authors used generative AI tools such as GPT only in limited sections to improve language and readability. The authors take full responsibility for the content of the manuscript.

Authors' contribution

Conceptualization, Tong Qu and Ke Sun; methodology, Tong Qu; software, Tong Qu; validation, Tong Qu and Ke Sun; formal analysis, Tong Qu; investigation, Tong Qu; resources, Tong Qu; data curation, Ke Sun; writing—original draft preparation, Tong Qu; writing—review and editing, Ke Sun; visualization, Tong Qu; supervision, Ke Sun; project administration, Ke Sun; funding acquisition, Ke Sun. All authors have read and agreed to the published version of the manuscript.

Conflicts of interest

The authors declare no conflicts of interest.

References

[1] Watkins N, Leighty B, Lipford W, Wong O, Goodman K, *et al.* Deployment of a pressure sensitive paint system for measuring global surface pressures on rotorcraft blades in simulated forward flight. In *Proceedings of the 28th Aerodynamic Measurement Technology, Ground Testing, and Flight Testing Conference*, New Orleans, USA, June 25–28, 2011, p. 2756.

[2] Watkins NA, Leighty DB, Lipford EW, Goodman ZK, Crafton J, *et al.* Measuring surface pressures on rotor blades using pressure-sensitive paint. *AIAA J.* 2015, 54(1):206–215.

[3] Luczak M, Dziedziech K, Vivolo M, Desmet W, Peeters B, *et al.* Contact versus non-contact measurement of a helicopter main rotor composite blade. In *Proceedings of the ISMA2010–USD2010 Conference*, Leuven, Belgium, September 20–22, 2010, pp. 352–360.

[4] Jahanmiri M. Pressure sensitive paints: the basics & applications. 2011. Available: https://publications .lib.chalmers.se/records/fulltext/140354.pdf (accessed on 15 October 2025).

[5] McLachlan BG, Bell JH. Pressure-sensitive paint in aerodynamic testing. Experimental thermal and fluid science. *Exp. Therm. Fluid Sci.* 1995, 10(4):470–485.

[6] Kasai M, Nagata T, Nonomura T. Indexes for evaluation of dynamic characteristics of pressure-sensitive paint based on pressure sensitivity and frequency response. *Meas. Sci. Technol.* 2024, 35(6):065101.

[7] Le Sant Y, Mérienne MC. Surface pressure measurements by using pressure-sensitive paints. *Aerosp. Sci. Technol.* 2005, 9(4):285–299.

[8] Klein C. Application of pressure sensitive paint (PSP) for the determination of the instantaneous pressure field of models in a wind tunnel. *Aerosp. Sci. Technol.* 2000, 4(2):103–109.

[9] Gregory JW, Asai K, Kameda M, Liu T, Sullivan JP. *et al.* A review of pressure-sensitive paint for high-speed and unsteady aerodynamics. *Proc. Inst. Mech. Eng, Part G: J. Aerosp. Eng.* 2008, 222(2):249–290.

[10] Scala G. Development of a pressure sensitive paint (PSP) measurement technique for high-speed turbine testing. Master's Thesis, Politecnico di Torino, 2021.

[11] Peng D, Liu Y. Fast pressure-sensitive paint for understanding complex flows: from regular to harsh environments. *Exp. Fluids* 2020, 61(1):8.

[12] Le Sant Y, Mérienne MC. Surface pressure measurements by using pressure-sensitive paints. *Aerosp. Sci. Technol.* 2005, 9(4):285–299.

[13] Watkins AN, Leighty BD, Lipford WE, Goodman KZ, Crafton J, *et al.* Measuring surface pressures on rotor blades using pressure-sensitive paint. *AIAA J.* 2016, 54(1):206–215.

[14] Soto-Valle R, Bartholomay S, Alber J, Manolesos M, Nayeri CN, *et al.* Determination of the angle of attack on a research wind turbine rotor blade using surface pressure measurements. *Wind Energy Sci.* 2020, 5(4):1771–1792.

[15] Chen D, Zhu H, Liu C, Li H, Li B, *et al.* Combined effects of unsteady wake and free-stream turbulence on turbine blade film cooling with laid-back fan-shaped holes using PSP technique. *Int. J. Heat Mass Transf.* 2019, 133:382–392.

[16] Yao Y, Zhu P, Tao Z, Song L, Li J, *et al.* Experimental study on the effects of slot jet on film cooling performance in the cascade endwall with purge flow. In *Proceedings of the ASME Turbo Expo 2019: Turbomachinery Technical Conference and Exposition*, Phoenix, USA, June 17–21, 2019.

[17] Cheng L, Wang R, Hao X, Liu G. Design of flexible pressure sensor based on conical microstructure PDMS-bilayer graphene. *Sensors* 2021, 21(1):289.

[18] Hilário J, Wang H, Wang P, Yu W, Meng C, *et al.* Modeling and simulation of microstructure geometry and material type on flexible capacitive pressure sensors by finite element analysis. *IEEE Sens. J.* 2024, 25(3):4811–4819.

[19] Gao J, Wang H, Gao Z, Gui H, Tang J, *et al.* Preparation and performance study of high-sensitivity flexible pressure sensors based on MXene/PVDF@ ZIF-8 composite membranes. *Appl. Surf. Sci.* 2025, 681:161626.

[20] Castaño Franco AF, Gallego Londoño J, Hernández Valdivieso AM. Test and fabrication of piezoresistive sensors for contact pressure measurements. *Rev. Fac. Ing. Univ. Antioquia* 2017, 82:47–52.

[21] Boukheddaden K, Ritti MH, Bouchez G, Sy M, Dîrtu MM, *et al.* Quantitative contact pressure sensor based on spin crossover mechanism for civil security applications. *J. Phys. Chem. C* 2018, 122(14):7597–7604.

[22] Wang S, Zhang S, Li X, Ren J. Optimization of the film cooling hole for minimizing stress concentration factor based on surrogate model. *Int. J. Heat Mass Transf.* 2024, 227:125546.

[23] Zhang J, Bhattacharya S, Vlachos PP. Using uncertainty to improve pressure field reconstruction from PIV/PTV flow measurements. *Exp. Fluids* 2020, 61(6):131.

[24] Van Gent PL, Michaelis D, Van Oudheusden BW, Weiss PÉ, Kat de R, *et al.* Comparative assessment of pressure field reconstructions from particle image velocimetry measurements and Lagrangian particle tracking. *Exp. Fluids* 2017, 58(4):33.

[25] Kaufmann R, Ganapathisubramani B, Pierron F. Full-field surface pressure reconstruction using the virtual fields method. *Exp. Mech.* 2019, 59(8):1203–1221.

[26] Qiu W, Sun Z, Wang J, Bai Y, Yao S, *et al.* A compressed sensing based framework for surface pressure field reconstruction from sparse measurement. *Phys. Fluids* 2025, 37(4):045109.

[27] Zhao X, Du L, Peng X, Deng Z, Zhang W, *et al.* Research on refined reconstruction method of airfoil pressure based on compressed sensing. *Theor. Appl. Mech. Lett.* 2021, 11(2):100223.

[28] Wang H, Wu F, Liu Y, He X, Wang S, *et al.* Machine-learning-based pressure reconstruction with moving boundaries. *J. Fluid Mech.* 2025, 1008:A21.

[29] Jafari M, Verma P, Zare A, Borghesani P, Bodisco TA, *et al.* In-cylinder pressure reconstruction by engine acoustic emission. *Mech. Syst. Signal Process.* 2021, 152:107490.

[30] Wang P, Hu G, Hu W, Xue X, Tao J, *et al.* Deep learning-based rapid flow field reconstruction model with limited monitoring point information. *Aerospace* 2024, 11(11):871.

[31] Huang Y, Zhu S, Chen S. Deep learning-driven super-resolution reconstruction of two-dimensional explosion pressure fields. *J. Build. Eng.* 2023, 78:107620.

[32] Zou J, Qiu W, Sun Z, Zhang X, Zhu X, *et al.* Joint optimization of sensor placement and sparse pressure field reconstruction with a two-stage framework for limited data. *Phys. Fluids.* 2025, 37(7):075231.

[33] Fan D, Xu Y, Wang H, Wang J. Comparative assessment for pressure field reconstruction based on physics-informed neural network. *Phys. Fluids* 2023, 35(7):075127.

[34] Li L, McClure J, Wright GB, Whitehead JP, Wang J, *et al.* Error propagation of direct pressure gradient integration and a Helmholtz-Hodge decomposition-based pressure field reconstruction method for image velocimetry. *Exp. Fluids* 2025, 66(5):1–24.

[35] Raissi M, Perdikaris P, Karniadakis GE. Physics-informed neural networks: a deep learning framework for solving forward and inverse problems involving nonlinear partial differential equations. *J. Comput. Phys.* 2019, 378:686–707.

[36] Karniadakis GE, Kevrekidis IG, Lu L, Perdikaris P, Wang S, *et al.* Physics-informed machine learning. *Nat. Rev. Phys.* 2021, 3(6):422–440.